Article

Structured Binder-Free Al-β Zeolite for Acid-Catalyzed Dehydration

Jiaxu Liu,* Shanshan Li, Zhenmei Zhang, Nicoletta Fusi, Chunyan Liu, Guang Xiong, Gianvito Vilé, and Ning He

Read Online

ACCESS | Metrics & More | Article Recommendations | Supporting Information

ABSTRACT: It has long remained a challenge in catalysis to synthesize technical hierarchical nanosized zeolites without growth modifiers and binders. Herein, we report a facile synthetic route to directly prepare binderless hierarchical Al-β zeolite in shaped form, with retained acidity, and sufficient mechanical strengths. The preparation process consists of two steps, where an Al-β zeolite nanopowder is first shaped using tetraethyl orthosilicate; the extrudate is then recrystallized under hydrothermal conditions with the assistance of tetraethylammonium hydroxide (TEAOH) solution. The alkaline environment leads to mesopores into the zeolite, and transforms as well the SiO₂ binders into a zeolite framework. Several characterization methods were performed to reveal the structure−property relationships of the materials in powdered and shaped form. It was found that the process of TEAOH treatment is the combination of desilication, mesopore formation, and binder recrystallization to give zeolite Al-β nanoparticles, resulting in the obvious increase in microporosity, acidity, and X-ray diffraction crystallinity of samples. Density functional theory calculations were also used to rationalize the recrystallization process. Finally, the utility of the materials was demonstrated by evaluating their catalytic properties in the dehydration of 2-(4-ethylbenzoyl)-benzoic acid, a reaction which is traditionally catalyzed by concentrated sulfuric acid and oleum. We found that the catalyst in technical form exhibits better catalytic performance than the powdered HB nanoparticles and higher product yield than traditional (homogeneous) catalysts.

KEYWORDS: Al-β zeolites, binders, full-crystalline monolithic zeolite Al-β, mesoporous materials, heterogeneous acid catalysis
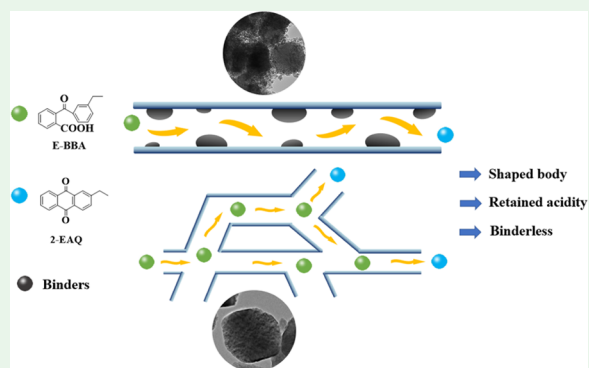
1. INTRODUCTION

Zeolites have been widely applied in industries because of their unique shape selectivity, excellent catalytic performance, and good hydrothermal stability.[1] In particular, zeolite β (*BEA type) possesses three-dimensional and intersected 12-membered ring pore channels, and is importantly used in the petrochemical and chemical industries. However, this traditional zeolite with a pore system of precisely narrowed microchannels could limit the mass transportation and the accessibility of molecules to the inner active sites, and this could lead to potential side reactions and sometimes even wreck the stability of catalysts.[2,3] Hierarchical zeolites with an additional mesopore and/or macropore network on top of and interconnecting with the micropores can maximize the application of porosity of zeolites, which hence have aroused widespread attention.[4−6] Typically, these methods can be divided into two categories: "top-down" and "bottom-up" approaches. Specifically, the top-down methods often consist in a secondary treatment of the synthesized zeolite using acid or alkali conditions; the bottom-up approaches usually need the addition of a special template during zeolite synthesis. At present, most of the research studies have focused on the preparation of hierarchical powder zeolites. However, powder zeolites cause pressure drop inside of the reactor. Thus, in practical application, structured zeolites (i.e., extrudates, pellets, monoliths, and granules) with sufficient mechanical strength are necessary, and this is done by adding binders (usually 30−50 wt %).[7−10] A few synthetic routes have been proposed to shape zeolite powders into technical form.[11,12] Unfortunately, the presence of binders in massive quantity end up covering the surface of the zeolites, blocking the channels and pores, and leading to additional diffusional limitation. This significantly affects the zeolite acidity, and generally has a negative impact on the catalytic performance, especially for acid-catalyzed reactions.[13−15]

In order to solve the abovementioned challenges, binderless zeolites are a technical solution.[16−18] For example, Wang et al.[16] successfully prepared a binderless ZSM-5 zeolite applied
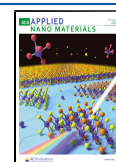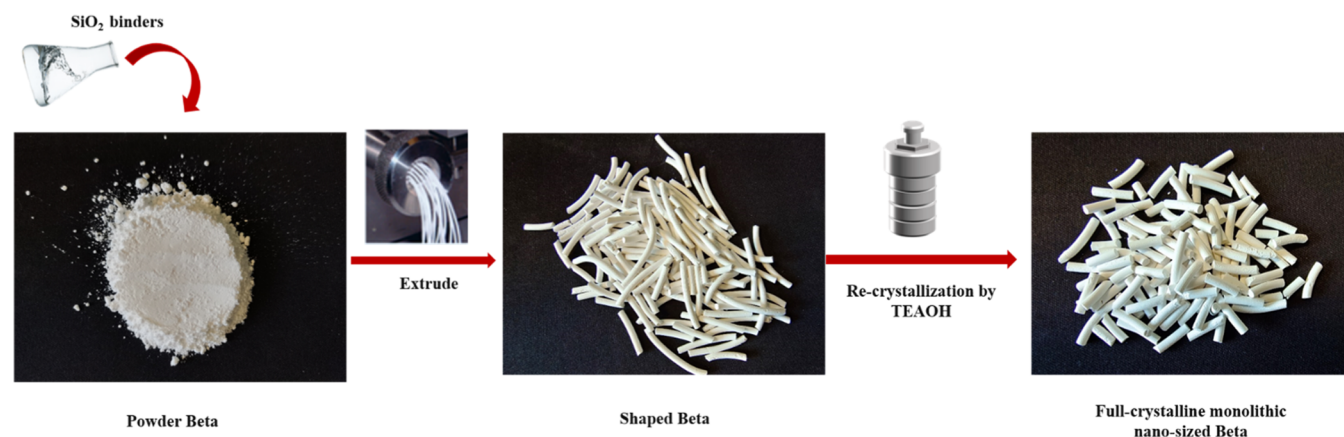
Scheme 1. Preparation Procedure of Hierarchical Nano-Sized Full-Zeolitic Monolith

in the dehydration of crude methanol to dimethyl ether reaction, which exhibited better catalytic performance and longer lifetime compared with traditional shaped catalysts with a binder. Some other groups have also reported the preparation of binderless ZSM-5 zeolite using dry gel conversion method, transforming the amorphous precursors into a ZSM-5 zeolite phase with the assistance of the organic structure-directing agents.[17,18] These investigations have pointed to the feasibility of obtaining binderless catalysts. Nevertheless, the amount of acid sites of the as-synthesized binderless samples significantly decreased compared with the parent powder zeolite.[19,20] Therefore, exploring a synthetic method to get structured zeolitic materials that not only maintain the textural and acidic properties of powdered zeolites but also have adequate mechanical strength has remained an unresolved challenge. However, this is of great importance for industrial application. Besides ZSM-5 zeolites, some other frameworks have also been explored, for example, the shaped binderless ZSM-11,[21] which showed a higher rate of formation of tert-butylamine than did the binder-containing catalysts; binderless zeolites 13X, 5A, and ZSM-5 made by 3D printing;[22] binderless zeolite NaX and A microspheres by using chitosan-assisted synthesis;[23−25] and one-pot synthesis route for preparing binderless zeolite A,[26] and so forth.

Trying to address this scientific gap, we reported herein the facile preparation method of a binder-free hierarchical Al-β zeolite in shaped form, whose size ranged from 200 to 300 nm. A series of characterization methods and density functional theory calculations were carried out to lift the veil of the structure−property relationships. Finally, the nano-sized materials were applied in the dehydration reaction of 2-(4-ethylbenzoyl)-benzoic acid (E-BBA), which traditionally is catalyzed by concentrated sulfuric acid and oleum. Compared with the traditionally homogeneous acid catalyst, the binder-free hierarchical nano-sized Al-β zeolite showed prominent advantages, such as shape selectivity, and stable hydrothermal stability.

2. MATERIALS AND METHODS

2.1. Catalyst Preparation. NH$_4$−Al-β zeolites (with particles of ca. 200−300 nm and total Si/Al ratio of 39) were supplied by Dalian Ligong Qiwangda Chemical Technology. H−Al-β zeolite (herein, indicated as HB) was obtained from the calcination of NH$_4$−Al-β zeolites under dry air at 540 °C for 6 h. HB zeolite (100 g) was mixed with tetraethyl orthosilicate (83.3 g, 20% aqueous solution), homogenized at room temperature in a speed mixer (SpeedMixer,

FlackTek Inc.), then extruded at room temperature into a uniform cylindrical body by rapid extrusion molding using a MiniScrew Extruder (Caleva, 2 mm cylindrical diameter), and dried at room temperature for 24 h. Subsequently, the extrudate was dried again at 110 °C for 12 h and subsequently calcined in air at 540 °C for 5 h, giving HBs.

To obtain hierarchical samples, the HB zeolite underwent an alkaline treatment in a 50 mL PTFE-lined stainless-steel autoclave using tetraethylammonium hydroxide solution (TEAOH, 40% aqueous solution). In particular, HBs (5 g) were mixed with a variable concentration of TEAOH solution (25, 50, 75, and 100 g), and the suspensions were then heated at 150 °C for 48 h to obtain HBs-05, HBs-10, HBs-15, and HBs-20, respectively. At the completion of this step, the product was washed, filtered, dried at 110 °C for 12 h, and subsequently calcined in air at 540 °C for 5 h. The preparation process is shown in Scheme 1.

2.2. Catalyst Characterization. X-ray diffraction (XRD) patterns of all powder samples (which were grounded into powder if it is shaped) were recorded using a Rigaku D/max-2004 diffractometer (Rigaku, Kyoto, Japan) with Cu Kα radiation (40 kV, 100 mA) and a 0.01° min^{-1} (2θ) scanning speed. To determine the total Si/Al ratio, inductively coupled plasma optical emission spectrometry (ICP OES) spectra were collected on a Spectro Arcos analyzer. We carried out transmission electron microscopy (TEM) and high-angle annular dark-field scanning transmission electron microscopy (HAADF-STEM) on a FEI (Tecnai F30 G2, The Netherlands) microscope. In order to study the tendency of the surface area and pore volumes, we conducted nitrogen physisorption on a Micromeritics ASAP 3020 instrument (Micromeritics, Atlanta, USA) at −196 °C. All samples were pretreated in vacuum at 350 °C for 5 h before the measurement. The surface area was determined by the Brunauer−Emmett−Teller (BET) method using the adsorption branch in the p/p_0 range from 0.05 to 0.35. The pore volumes were evaluated at p/p_0 of 0.99, while micro- and mesoporosity were discriminated using the t-plot method. Ammonia temperature-programmed desorption (NH$_3$-TPD) was used to qualitatively analyze the tendency of the overall acidity of samples. The profiles were carried out on a Quantachrome ChemBET 3000 chemisorb instrument. The samples (0.14 g, ca. 20−40 mesh) were loaded into a quartz U-reactor and degassed in helium for 1 h, and then, the temperature was cooled to 150 °C for 30 min NH$_3$ adsorption. Then, we removed the weakly adsorbed NH$_3$ by a constant helium purging after the initial adsorption. Taking helium in 20 mL min^{-1} as a carrier gas, desorption was recorded from 150 to 600 °C at a rate of 15 °C min^{-1}. Fourier transform infrared spectroscopy (FTIR) was employed to distinguish the acid sites of different samples. The spectra for surface hydroxyl (OH) vibrations and pyridine adsorption were recorded with a Nicolet 10 FTIR spectrometer ranged from 4000 to 400 cm^{-1} with an optical resolution of 4 cm^{-1}. The detailed measurement process has been reported in our previous work.[36] Solid-state nuclear magnetic resonance experiments were carried out on an Agilent DD2-500

MHz spectrometer (Agilent Technologies Inc, California, USA). In particular, ^{29}Si magic angle spinning nuclear magnetic resonance (MAS NMR) experiments were performed with a 4 s repetition time, 4000 scans, and contact time of 1.5 ms. The ^{29}Si spectra were referenced to 4,4-dimethyl-4-silapentane sulfonate sodium. ^{27}Al MAS NMR spectra were acquired at 130.2 MHz using a 4 mm MAS NMR probe with 14 kHz spinning speed. The ^{27}Al spectra were referenced to 1% $Al(NO_3)_3$ aqueous solutions. The microcomputational tomography (microCT) of the shaped bodies was performed in a BIR Actis 130/150. The generator and detector were fixed, while the sample was rotated; the scanning plane was horizontal. The X-ray spectra were collected on a flat panel detector, which converted the collected spectra in raw data and sent them to the computer, where they were processed as black/white images. The voxel of the images here presented is $7 \times 7 \times 7 \ \mu m$. Segmentation of 2D slices obtained from the microCT technique was carried out by means of AvizoMercury software. The mechanical resistance (or crushing strength) of the shaped zeolites was measured using the Instron 5.965 system (Instron). The shaped zeolite was positioned between the compressing disks of the system and subjected to an increasing load until breakage. The force applied at the breaking point was registered with an accuracy of 0.2%.

2.3. Catalyst Performance. Dehydration reaction of E-BBA (density 1.1783) was carried out under atmospheric pressure in a batch reactor. In a typical experiment, E-BBA (2 g) was loaded into the reactor (25 mL) under neat conditions (i.e., without any solvent) and heated to reach the reaction temperature (210 °C). At this stage, E-BBA (melting point 138 °C, boiling point 343 °C) was completely solubilized. Preliminary quantitative high-pressure liquid chromatography (HPLC) analysis of the liquid ensured no degradation of the starting materials at this stage. Then, under vigorous stirring (500 rpm), the shaped zeolite catalyst (2 g, which was sieved into 20−40 mesh) was added, and the suspension was kept at the reaction temperature for 60 min. Upon completion of this step, an aliquot of the reaction solution was collected and immediately analyzed by HPLC (Waters 1525, SunFire C_{18} column, 5 μm, 150 × 4.6 mm). The liquid phase was the mixture of H_2O, CH_3OH, and tetrahydrofuran (1:1:1 volumetric ratio) at a flowing rate of 0.5 mL min^{-1}. The UV detector of the HPLC was set at 274 nm wavelength. The calibration curves were linear for E-BBA ($R^2 = 0.9995$) and 2-EAQ ($R^2 = 0.9997$).

2.4. Density Functional Theory Calculations. To understand the crystallization process, a periodic supercell (1 × 2×1) was used to represent the zeolite topology (Figure 1). The crystallographic

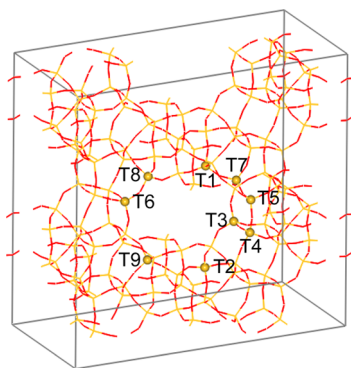**Figure 1.** Periodic supercell (1 × 2×1) representing the Al-β zeolite topology.

structure of β was taken from the database maintained by the International Zeolite Association. All periodic DFT calculations were conducted with the CASTEP code in Materials Studio. We used generalized gradient approximation of PBE form to describe electron exchange and correlation. Ultrasoft pseudopotentials and a plane wave cutoff energy of 400 eV were used for core and valence states, respectively. All calculations were performed spin polarized and van

der Waals forces. We converged self-consistent field electronic energies to 5×10^{-7} eV $atom^{-1}$ and atomic forces for geometric relaxation using the conjugate gradient algorithm to less than 0.02 eV $Å^{-1}$. The Gamma point was used to sample the surface Brillouin zone.

3. RESULTS AND DISCUSSION

Table 1 outlines the textural properties of all samples. The total Si/Al ratio is 39 over the HB sample; this value first increases over HBs, due to the presence of a siliceous binder, and then drops upon increasing the concentration of the base during alkaline treatment, reaching a final Si/Al ratio of 32 over HBs-20. The textural properties of the samples are also affected by the extrusion and TEAOH treatment: the increased mesopore surface area passes from 95 in HB to 138 $m^2 \ g^{-1}$ in HBs-15 and to 153 $m^2 \ g^{-1}$ in HBs-20. This corresponds to a 60% mesopore surface area increase between the first and the last sample. In line with previous observations,[13−15] the slight drop in S_{meso} observed over HBs-05 and HBs-10 is likely due to the presence of the binder blocking the surface of the catalyst. The increase in mesoporosity is obviously observed by the pore volume data because V_{meso} changes from 0.11 in HB to 0.18 $m^2 \ g^{-1}$ in HBs-20, in accordance with ca. 60% increase. In addition, compared with traditional shaped sample HBs, the crushing strength of all shaped samples after TEAOH treatment is increased after sharing, meeting industrial strength requirements (>10 N mm^{-1}).

Figure 2a,b shows the N_2 isotherms and corresponding pore size distribution of all samples, respectively. Based on the shape, the isotherm of HB can be attributed to a type-I, indicating the material consisting of micropores and limited mesopores. Meanwhile, for HBs, HBs-15, and HBs-20, a composite of typical type-I and type-IV with a H1 hysteresis loop can be observed, indicating the existence of relatively more mesopores. Moreover, the pore size distribution (Figure 2b) indicates that the mesopores are bimodal with pore sizes of ca. 3.8 and 6−12 nm. Concerning the peak centered at 3.8 nm, this has been observed elsewhere and indicates that the zeolite contains internal mesopores connected to the surface via micropores (probably those of the β zeolite itself). On the other hand, there is a trend that the size of larger mesopores was gradually increased from 6 to 12 nm, as the concentration of TEAOH solution increased. The formation of mesopores after TEAOH treatment is corroborated by the micrographs shown in Figures 3a and S1. Figure 3a, in particular, shows the slow transformation of the amorphous binder and the presence of mesopores in the crystals. Also, Figure 3b highlights the consistency of the observed average mesopore size with the pore size distribution shown in Figure 2. Finally, energy-dispersive system (EDS) maps show the very uniform distribution of Si and Al species in the HBs-2.0 sample, which would be unexpected when a purely siliceous binder (SiO_2, came from the calcination of tetraethyl orthosilicate sol) is also present in the sample (Figure 3c). Based on the overall composition and textural analysis, we can state that the shaping process increases the Si/Al content and slightly reduces S_{BET} and pore volume due to the existence of the SiO_2 binder that covers also the surface sites of zeolite. After TEAOH treatment and calcination, the micrographs show no areas of higher concentration of Si, together with an increase of mesopore surface area and Si/Al reduction. These data indicate a partial desilication of the zeolite, but they are not conclusive whether the binder is also removed via desilication or rather

Table 1. Composition and Texture Properties of All Samples

catalyst[a]	Si/Al[b]	S_{BET}[c] (m² g⁻¹)	S_{meso}[d] (m² g⁻¹)	V_{pore}[e] (cm³ g⁻¹)	V_{micro}[d] (cm³ g⁻¹)	V_{meso}[f] (cm³ g⁻¹)	crushing strength (N mm⁻¹)
HB	39	614	95	0.33	0.22	0.11	
HBs	42	557	113	0.31	0.18	0.13	5
HBs-05	40	530	70	0.30	0.20	0.10	11
HBs-10	34	612	64	0.30	0.24	0.06	12
HBs-15	33	687	138	0.35	0.23	0.12	12
HBs-2 0	32	671	153	0.40	0.22	0.18	14

[a]Descriptions of the acronyms are given in the Materials and Methods. [b]Si/Al by ICP-OES. [c]BET method. [d]t-plot method applied to the N₂ isotherm. [e]V_{pore} was calculated from N₂ adsorbed at $p/p_0 = 0.99$. [f]$V_{meso} = V_{pore} - V_{micro}$.
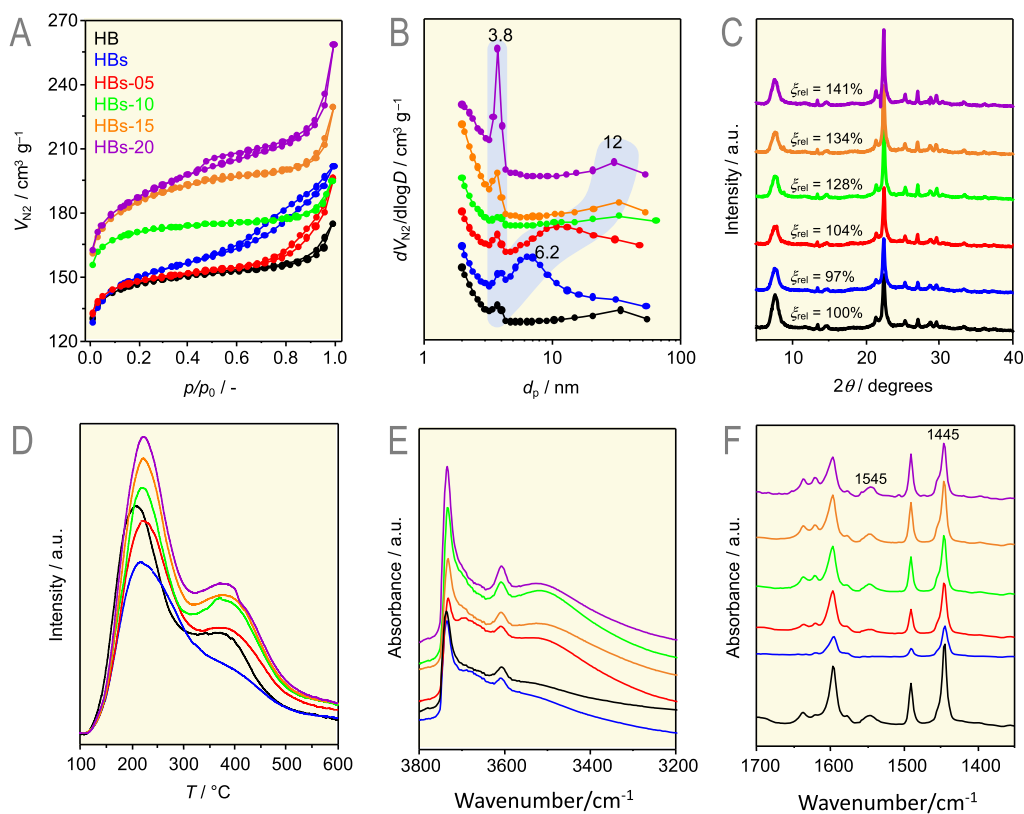

Figure 2. Characterization of all samples. N₂ adsorption−desorption isotherms at −196 °C (a), corresponding pore size distribution by BJH (b), XRD patterns with relative crystallinity (c), NH₃-TPD profile (d), and FTIR-OH (e) and FTIR-pyridine (f).

recrystallizes in some other forms. To address this point, we have conducted additional characterizations.

In particular, the XRD patterns of all samples are shown in Figure 2c. Six characteristic diffraction peaks of Al-β zeolite can be seen in all samples, and the crystallinity can thus be calculated by the sum of areas of these peaks.[27,28] Taking the crystallinity (ξ, 100%) of HB as a reference, the relative crystallinity (ξ_{rel}) of other samples was calculated. For that matter, HBs have the lowest crystallinity of 97%, in line with the fact that an amorphous binder is present. Then, the crystallinity linearly increases with the TEAOH treatment. In particular, HBs-15 and HBs-20 have much higher relative crystallinity than HB. This increase in crystallinity is surprising and, if the base treatment is responsible for the observed formation of mesopores and eventually for the destruction of the siliceous binder, we would expect a reduction of the sample crystallinity after TEAOH treatment, mainly because the alkaline treatment has partially "destroyed" the framework. Instead, the increased crystallinity (and the absence of any other reflection assigned to other phases, such as pure SiO₂)

can be explained, suggesting that the amorphous silica binder in HBs, in the presence of TEAOH and at high temperature, has recrystallized into an Al-β zeolite phase. In fact, no significant structure damage after the treatment and no other peaks assigned to side frameworks can be identified. This aspect is not surprising, considering that, under the experimental conditions, TEAOH is known to act as a structure directing agent in the solution and in the alkaline environment and the SiO₂ binder initiates the secondary crystallization to give Al-β zeolite.

To obtain deeper insights into the Al distribution and location,[34] ²⁹Si and ²⁷Al MAS NMR data were obtained (Figure 4), while the ²⁷Al MQ MAS NMR plots are shown in Figure S2. The results further prove that the framework Al species increased after TEAOH. In particular, the spectra show a single broad signal in the isotropic dimension corresponding to four-coordinate Al species in the framework. It is interesting to note that the ²⁷Al NMR intensity of HBs-20 is very small compared to HB, indicating that the TEAOH treatment was not only desilication but also dealumination at the same time.
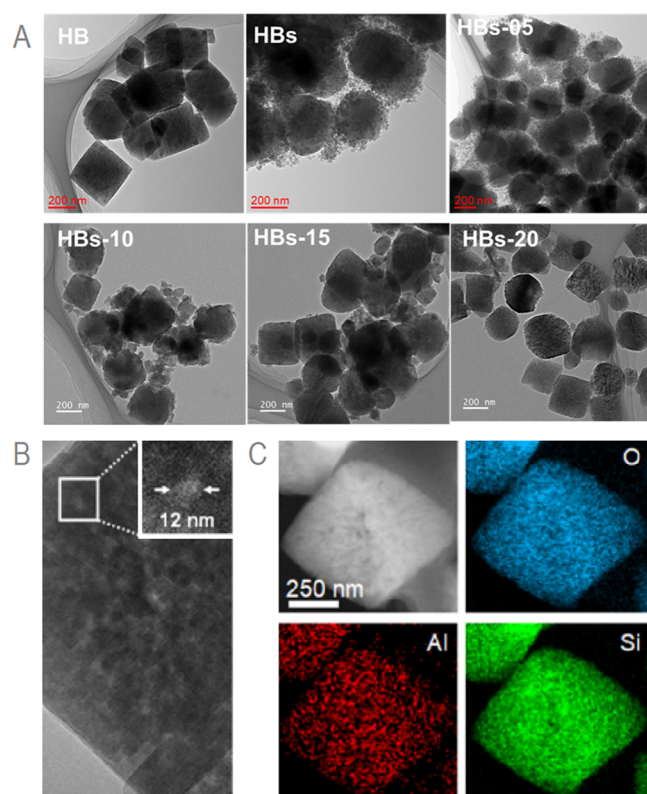
Figure 3. TEM micrographs of all samples. (a) HRTEM micrograph of HBs-20 with characteristic mesopores. (b) STEM and EDS mapping of oxygen, aluminum, and silicon of HBs-20 (c).
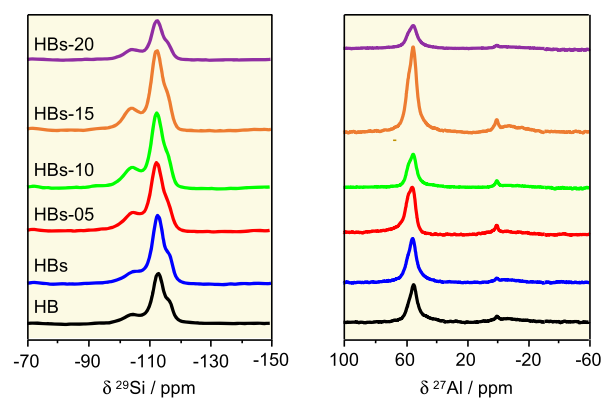

Figure 4. ^{29}Si (left) and ^{27}Al (right) MAS NMR spectra of all samples.

3.1. Acid−Base Characterization. It is often essential to characterize the acidity of the samples because most of the industrial reactions utilize the acidic sites of zeolites, and the purpose of this study is to restore the acidity of shaped zeolites. The acidity has been determined by NH_3-TPD profiles and FTIR spectra. As shown in Figure 2d, the desorption peaks at 200−220 and 350−400 °C correspond to weak and strong acid sites, respectively.[29] Compared to HB, the intensity of the two desorption peaks in HBs both decreased because of the addition of the silica binder, which dilutes the acid sites. Especially compared with the results of NH_3, as we can see from Table 2, the values of pyridine adsorption decreased more significantly, indicating the decreased accessibility of acid sites, which have been blocked by the binder. After TEAOH treatment, the total acidity of zeolite is restored, especially for pyridine adsorption. Considering the size of molecules (NH_3 and pyridine), it was deduced that the combination of desilication and conversion of the binder into zeolite Al-β structure mainly improves the unobstructed pore channel of the formed nano-sized zeolites and the accessibility of acid sites. In HBs-20, the acidity recover, and even to the extent that the adsorption value for NH_3 was increased, which can be attributed to additional aluminum sources that transform into Al sites in the framework during TEAOH treatment.

As shown in Figure 2e, we have studied the hydroxyls (−OH) related to Brønsted acidity (3600 and 3550 cm^{-1}) and those representative of isolated silanols on the external surface (3740 cm^{-1}).[30,31] The structured HBs display a reduced intensity of 3610 cm^{-1} related to Brønsted acidity compared to the parent nano-sized HB, which correspond to the lower Al content resulting from the abundant binders and the formation of Al-rich debris, respectively. After TEAOH treatment (e.g., HBs-15 and HBs-20), the bands at 3740 cm^{-1} become prominent, indicating the presence of substantial defects because of the hierarchical structure.[30,31] At the same time, the intensity of 3610 cm^{-1} has the tendency to grow back, indicating that the Brønsted sites are gradually recovered due to the transformation of the SiO_2 binder into the zeolite framework and realumination due to TEAOH.[30,31] To further confirm our conclusions, we have used pyridine as a probe molecule, which could distinguish the internal and external surface acidity, to investigate the overall acid sites in different positions of zeolites. As we can see from Figure 2f, all spectra display three peaks at 1545, 1445, and 1633 cm^{-1}, which are ascribed to Brønsted acid sites, Lewis acid sites, and Brønsted acid sites on the external surface, respectively. Owing to the massive inert binders, which could cover the external surface and dilute the acid sites, all peaks in HBs drastically decreased compared with parent powder zeolites. On the other hand, the

Table 2. Amount and Distribution of Acid Sites on the Materials

catalyst	NH$_3$ adsorption			pyridine adsorption		
	C_w^a (mmol g^{-1})	C_s^b (mmol g^{-1})	Cw/Cs (−)	C_{BS}^c (μmol g^{-1})	C_{LS}^d (μmol g^{-1})	C_{BS}/C_{LS} (−)
HB	0.28	0.29	0.97	160	347	0.46
HBs	0.24	0.23	1.04	15	153	0.10
HBs-05	0.24	0.34	0.71	66	235	0.28
HBs-10	0.31	0.27	1.15	109	252	0.43
HBs-15	0.34	0.27	1.26	123	282	0.44
HBs-20	0.35	0.30	1.17	143	263	0.54

^{a}Amount of NH_3 adsorbed on weak acid sites. ^{b}Amount of NH_3 adsorbed on strong acid sites. ^{c}Amount of pyridine adsorbed on Brønsted acid sites. ^{d}Amount of pyridine adsorbed on Lewis acid sites.

intensity of the samples after TEAOH treatment increased obviously, indicating the recovery of acidity, especially for HBs-15 and HBs-20, which confirmed the transformation of amorphous inert binders into the zeolite phase and the redistribution of aluminum sources, in line with above-mentioned conclusions. Such redistribution is verified by the EDS micrographs shown in Figure 3c, which show no preferential locations for the Al atoms and homogeneous Al distribution.

Overall, this combination of results over the powdered materials suggests a combination of desilication, mesopore formation, and binder recrystallization to give zeolite Al-β, whose size ranged from 200 to 300 nm. In fact, if the secondary crystallization would not happen, the microporosity, acidity, and XRD crystallinity would decrease rather than increase. Hence, the samples are made by the cooperation between secondary crystallization and OH$^-$ desilication. In summary, TEAOH solutions played a dual role in the post-treatment. On the one hand, OH$^-$ of TEAOH could dissolve Si species of parent-shaped Al-β; on the other hand, TEA$^+$ of TEAOH can promote recrystallization as a template. These two completely reverse effects are in dynamic equilibrium.[35] The concentration of TEAOH solutions significantly affects the pore structure properties of zeolite crystals. Moderate concentration TEAOH solutions tend to perform recrystallization effects with parent β as seeds and transformed dissolved Si species into the zeolite phase, contributing to a new zeolite shell. Therefore, at appropriate concentration of TEAOH solutions, desilication and recrystallization occurred simultaneously, and the rate of mesopore formation and crystal growth would reach to some extent balance. Specifically, the number of micropores exceeds parent powder Al-β, while the number of mesopores increases. At this point, if the concentration of TEAOH continues to increase, the desilication will be deepened resulting in the increasing number of mesopores at the expense of micropores.[35]

3.2. Characterization of the Shaped Bodies.
Characterization of the shaped bodies was also undertaken to understand the distribution of the macropores and analyze the mechanical stability of the materials. In particular, microCT images (Figure 5) for HBs-20 reveal irregular macropores (in blue on the left image and in black on the right micrograph), which are well distributed over the whole sample. The pores have elongated to sub-rounded shape and appear to be accessible from the surface. The macroporosity is ca. 3% of the whole volume. Recrystallization of amorphous SiO_2 binders into
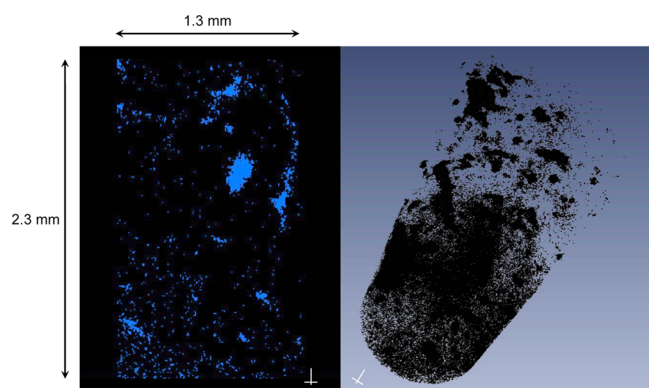

1.3 mm

2.3 mm

Figure 5. X-ray tomography micrographs of HBs-20 in shaped form.

crystalline zeolite improves the mechanical strength of the samples as well, as shown in Table 1, where the crushing strength goes from 5 N mm^{-1} of HBs to 14 N mm^{-1} over HBs-20. In summary, the shaping and alkaline process with TEAOH improves the diffusion property due to the formation of macro, meso, and micropores, as well as the mechanical strength.

3.3. Zeolite Recrystallization Mechanism.
To further understand the recrystallization process, we performed plane-wave, supercell DFT calculations, studying the position of Si or Al rearranged into the zeolite framework. In particular, the location energies of Si or Al in different T sites and the adsorption energy of NH_3 of the obtained different sites to determine the acidity of the corresponding bridged hydroxyl group were calculated. As shown in Figure 6a, the location
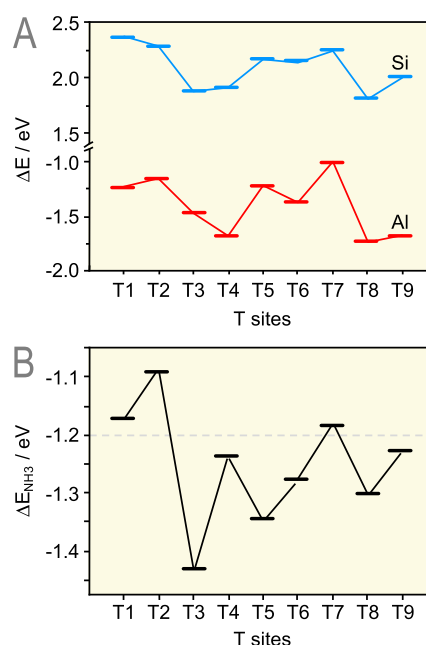

Figure 6. Location energies of Si or Al (a) and adsorption energies of NH_3 (b) for different T sites in β zeolites during the recrystallization process.

energies of Al were more negative than those of Si, indicating that, during the possible recrystallization, Al is more favorable to get into the framework of the zeolite. More importantly, it was found that for nine different T sites of Al-β, the Al location can be divided into two groups: (i) T1, T2, and T7, located in a five-membered ring linked to two channels of zeolite, which have relatively high location energies and low Brønsted acidity (Figure 6b); (ii) T3−T6, T8, and T9, most of which located at intersection of channels with good accessibility, and have lower location energies and high Brønsted acidity. Based on this analysis, the latter T sites (T3−T6, T8 and T9) tend to rearrange aluminum sources into the framework from a thermodynamic viewpoint and the resulting acidity is higher. The calculated results corroborate that, under the experimental conditions and in the presence of the siliceous binder, the aluminum source in TEAOH can effectively be transformed into framework Al and the acidity of zeolites is increased.

3.4. Application in Heterogeneous Acid Catalysis.
The structured binder-free Al-β zeolite nanoparticles were applied in the dehydration reaction of E-BBA to 2-ethyl-anthraquinone (2-EAQ) performed at atmospheric pressure in a flask.[32,33] This reaction is very important for the synthesis of

fine chemicals and pharmaceuticals, which is traditionally catalyzed by concentrated sulfuric acid and oleum catalysts leading to severe environmental pollution and unsatisfactory yield. In fact, the 2-EAQ product is an important raw material used in the synthesis of hydrogen peroxide (H_2O_2). Hydrogen peroxide (H_2O_2) is a highly efficient and green oxidant because it has the highest content of active oxygen. As a result, the demand of 2-EAQ worldwide in 2021 is more than 40000 tons and expected to increase at the rate of 8%. The most widely applied industrial synthetic route for producing 2-EAQ is the phthalic anhydride method using concentrated sulfuric acid or oleum as a catalyst. This process, however, suffers from environmental post-treatment problem. Therefore, under the dual pressure of fast-growing demand of 2-EAQ and environmental protection, producers eagerly need a new environmental benign catalyst to replace the concentrated sulfuric acid and oleum catalysts.

In general, the dehydration reaction of E-BBA catalyzed by sulfuric acid and the oleum catalyst, even though they could produce the desired products by intramolecular dehydration, they also unavoidably give undesired oligomers or other byproducts resulting from lack of shape selectivity, which thus cause unsatisfied yield (below 30%) to 2-EAQ.[32,33] On the contrary, our structured binder-free Al-β zeolite nanoparticles showed excellent catalytic performance. As shown in Figure 7,
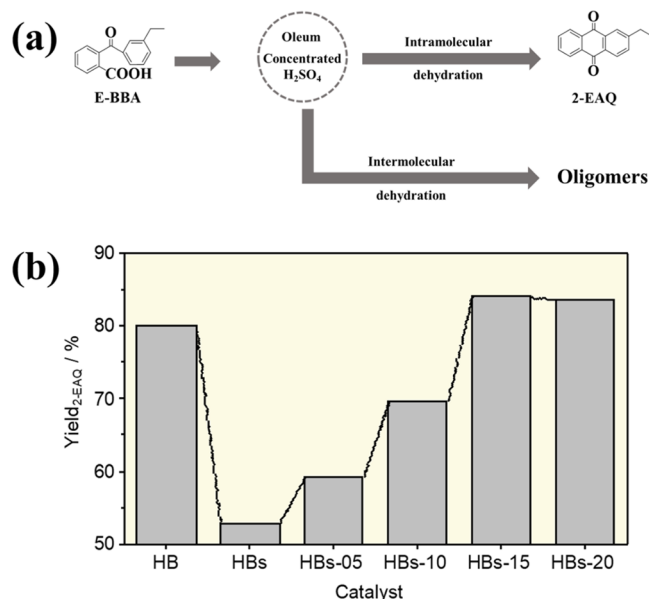

Figure 7. Reaction scheme for E-BBA dehydration (a), yield to 2-EAQ product over all samples. (b) Reaction conditions: temperature 210 °C, 1 bar, catalyst 2.0 g, E-BBA 2.0 g, reaction time 60 min.

the yield to the desired 2-EAQ product dropped dramatically from approximately 80% in the parent powder HB catalyst to 53% in the shaped HBs containing massive binders, while for catalysts hydrothermally treated by TEAOH solutions, the yield of 2-EAQ could be gradually improved. It was worth mentioning that the catalytic performance of HBs-15 and HBs-20 was improved even better than parent powder HB, which strongly proved the unique advantages of the abovementioned samples compared to traditional (homogeneous) catalysts and could be applied in the industrial reactions catalyzed by acid sites.

This result is confirmed plotting the conversion of E-BBA and the selectivity to 2-EAQ (Figure S3). DFT calculations were carried out to get the energy profile for E-BBA intramolecular dehydration over Al-β and uncover the type of active sites involved in the process. The reaction path is shown in Figure S4; it starts with the E-BBA physical adsorption, followed by a C−H bond cleavage, giving adsorbed 2-EAQ and H_2O products, which desorb. In particular, the O−H bond formation takes place between the C=O group of the E-BBA molecule and H^+ on H-β zeolite. The first intermediate has to go through a large transition state (TS_1) through H transfer from the C−H bond of ethylbenzene to the O atom of C=O, forming a C−C bond. This step is rate-determining due to its large intrinsic activation barrier ($\Delta E = 51.92$ kcal mol^{-1}). However, it is crucial to highlight that the acidity of the catalyst is critical to the reaction because it plays a key role in the H transfer from the C−H bond of ethylbenzene to the O atom of C=O, suggesting that the framework aluminum species with strong Brønsted acidity are active sites in E-BBA intramolecular dehydration.

4. CONCLUSIONS

In our report, we have developed a facile synthetic route for the preparation of structured binder-free Al-β zeolite with retained acid sites and sufficient mechanical strength, through a process that involves mesopore formation and binder recrystallization to give zeolite Al-β. We have studied the physicochemical properties of the powdered and structured samples through a variety of characterization methods, such as N_2 physisorption, IR, NMR, XRD, (S)TEM, NH_3-TPD, and X-ray tomography. DFT calculations corroborate that, under the experimental conditions and in the presence of the siliceous binder, the aluminum source in TEAOH can effectively be transformed into framework Al, which well explains the reason of the increased acidity of zeolites after TEAOH treatment. We chose the dehydration reaction of E-BBA as probe reaction to evaluate the catalytic performance of all samples. Satisfactorily, the as-synthesized nanoparticle samples showed outstanding catalytic performance with excellent yield of production 85%, which was far higher than the traditional acid catalyst due to their unique shape selectivity, retained acidity, developed textural structure, and sufficient mechanical strength. We strongly believe that our results provide insights into the preparation and optimization of zeolite catalysts with practical applications and fundamentally uncover the mechanism consisting of binder migration into the framework and acidity recovery.

■ ASSOCIATED CONTENT

ⓢ Supporting Information

The Supporting Information is available free of charge at https://pubs.acs.org/doi/10.1021/acsanm.1c02559.

Additional characterization data of the materials (PDF)

■ AUTHOR INFORMATION

Corresponding Author

Jiaxu Liu − *State Key Laboratory of Fine Chemicals, Department of Catalytic Chemistry and Engineering, Dalian University of Technology, 116024 Dalian, China;* ⓞ orcid.org/0000-0003-0815-3979; Email: liujiaxu@dlut.edu.cn

Authors

Shanshan Li − *State Key Laboratory of Fine Chemicals, Department of Catalytic Chemistry and Engineering, Dalian University of Technology, 116024 Dalian, China*

Zhenmei Zhang − *State Key Laboratory of Fine Chemicals, Department of Catalytic Chemistry and Engineering, Dalian University of Technology, 116024 Dalian, China*

Nicoletta Fusi − *Earth and Environmental Sciences Department, Università degli Studi Milano-Bicocca, 20126 Milano, Italy*

Chunyan Liu − *State Key Laboratory of Fine Chemicals, Department of Catalytic Chemistry and Engineering, Dalian University of Technology, 116024 Dalian, China*

Guang Xiong − *State Key Laboratory of Fine Chemicals, Department of Catalytic Chemistry and Engineering, Dalian University of Technology, 116024 Dalian, China*

Gianvito Vilé − *Department of Chemistry, Materials, and Chemical Engineering "Giulio Natta", Politecnico di Milano, 20133 Milano, Italy;* orcid.org/0000-0003-0641-8590

Ning He − *State Key Laboratory of Fine Chemicals, Department of Catalytic Chemistry and Engineering, Dalian University of Technology, 116024 Dalian, China*

Complete contact information is available at:
https://pubs.acs.org/10.1021/acsanm.1c02559

Author Contributions

The manuscript was written through contributions from all authors and everyone gave approval to the final version of the manuscript.

Notes

The authors declare no competing financial interest.

■ REFERENCES

(1) Chen, L.-H.; Sun, M.-H.; Wang, Z.; Yang, W.; Xie, Z.; Su, B.-L. Hierarchically Structured Zeolites: From Design To Application. *Chem. Rev.* **2020**, *120*, 11194.

(2) Hu, G.; Yang, J.; Duan, X.; Farnood, R.; Yang, C.; Yang, J.; Liu, W.; Liu, Q. Recent Developments And Challenges In Zeolite-Based Composite Photocatalysts For Environmental Applications. *Chem. Eng. J.* **2021**, *417*, 129209.

(3) Zhu, Z.; Xu, H.; Jiang, J.; Wu, H.; Wu, P. Hydrophobic Nanosized All-Silica Beta Zeolite: Efficient Synthesis and Adsorption Application. *ACS Appl. Mater. Interfaces* **2017**, *9*, 27273−27283.

(4) Luo, W.; Cao, W.; Bruijnincy, P. C. A.; Lin, L.; Wang, A.; Zhang, T. Zeolite-Supported Metal Catalysts For Selective Hydrodeoxygenation Of Biomass-Derived Platform Molecules. *Green Chem.* **2019**, *21*, 3744.

(5) Pan, M.; Zheng, J.; Liu, Y.; Ning, W.; Tian, H.; Li, R. Construction And Practical Application Of A Novel Zeolite Catalyst For Hierarchically Cracking Of Heavy Oil. *J. Catal.* **2019**, *369*, 72−85.

(6) Feliczak-Guzik, A. Hierarchical Zeolites: Synthesis And Catalytic Properties. *Microporous Mesoporous Mater.* **2018**, *259*, 33−45.

(7) Mendes, P. S. F.; Silva, J. M.; Ribeiro, M. F.; Daudin, A.; Bouchy, C. From Powder To Extrudate Zeolite-Based Bifunctional Hydroisomerization Catalysts: On Preserving Zeolite Integrity And Optimizing Pt Location. *J. Ind. Eng. Chem.* **2018**, *62*, 72−83.

(8) Tao, Y.; Kanoh, H.; Abrams, L.; Kaneko, K. Mesopore-Modified Zeolites: Preparation, Characterization, And Applications. *Chem. Rev.* **2006**, *106*, 896−910.

(9) Bingre, R.; Louis, B.; Nguyen, P. An overview on zeolite shaping technology and solutions to overcome diffusion limitations. *Catalysts* **2018**, *8*, 163.

(10) Kwon, S. H.; Lee, S. Y.; Kim, H.-J.; Kim, H.-T.; Lee, S. G. Molecular Dynamics Simulation To Reveal Effects Of Binder Content On Pt/C Catalyst Coverage In A High-Temperature Polymer Electrolyte Membrane Fuel Cell. *ACS Appl. Nano Mater.* **2018**, *1*, 3251.

(11) Wang, D.; Liu, Z.; Wang, H.; Xie, Z.; Tang, Y. Shape-Controlled Synthesis Of Monolithic ZSM-5 Zeolite With Hierarchical Structure And Mechanical Stability. *Microporous Mesoporous Mater.* **2010**, *132*, 428.

(12) Ivanova, S.; Louis, B.; Madani, B.; Tessonnier, J. P.; Ledoux, M. J.; Pham-Huu, C. ZSM-5 Coatings on β-SiC Monoliths: Possible New Structured Catalyst for the Methanol-to-Olefins Process. *J. Phys. Chem. C* **2007**, *111*, 4368.

(13) Yang, K.; Zhang, D.; Zou, M.; Yu, L.; Huang, S. The Known and Overlooked Sides of Zeolite-Extrudate Catalysts. *ChemCatChem* **2021**, *13*, 1414−1423.

(14) Shen, Z.; Ma, C.; He, J.; Wang, D.; Sun, H.; Zhu, Z.; Yang, W. Preparation Of A Shaped Core-Shell Structured Binder-Free ZSM-5 Catalyst And Its Application For Benzene Alkylation With Ethylene. *Appl. Catal., A* **2019**, *577*, 20.

(15) Hargreaves, J. S. J.; Munnoch, A. L. A Survey Of The Influence Of Binders In Zeolite Catalysis. *Catal. Sci. Technol.* **2013**, *3*, 1165−1171.

(16) Zhou, J.; Teng, J.; Ren, L.; Wang, Y.; Liu, Z.; Liu, W.; Yang, W.; Xie, Z. Full-Crystalline Hierarchical Monolithic ZSM-5 Zeolites As Superiorly Active And Long-Lived Practical Catalysts In Methanol-To-Hydrocarbons Reaction. *J. Catal.* **2016**, *340*, 166.

(17) Yan, B.; Yu, S.; Zeng, C.; Yu, L.; Wang, C.; Zhang, L. Binderless zeolite NaX microspheres with enhanced CO_2 adsorption selectivity. *Microporous Mesoporous Mater.* **2019**, *278*, 267.

(18) Jiang, H.; Wang, D.; Tan, J.; Chen, Y.; An, Y.; Chen, Y.; Wu, Y.; Sun, H.; Shen, B.; Wu, D.; Liu, J.; Ling, H.; Zhao, J.; Tong, Y. In Situ Hydrothermal Conversion Of Silica Gel Precursors To Binderless Zeolite X Pellets For Enhanced Olefin Adsorption. *Ind. Eng. Chem. Res.* **2020**, *59*, 9997.

(19) Liu, D.; Li, G.; Liu, J.; Wei, Y.; Guo, H. Mesoporous Titanium-Silicalite Zeolite Containing Organic Templates as a Bifunctional Catalyst for Cycloaddition of CO2 and Epoxides. *ACS Appl. Mater. Interfaces* **2018**, *10*, 22119.

(20) Shang, C.; Wu, Z.; Wu, W. D.; Chen, X. D. Chemical Crosslinking Assembly Of ZSM-5 Nanozeolites Into Uniform And Hierarchically Porous Microparticles For High-Performance Acid Catalysis. *ACS Appl. Mater. Interfaces* **2019**, *11*, 16693−16703.

(21) Zhang, W.; Zhang, S.; Xin, W.; Liu, H.; Shang, Y.; Zhu, X.; Liu, S.; Xu, L. Shaped binderless ZSM-11 zeolite catalyst prepared via a dry-gel conversion method: Characterization and application for alkylation of benzene with dimethyl ether. *J. Energy Chem.* **2017**, *26*, 380−389.

(22) Lawson, S.; Newport, K.; Al-Naddaf, Q.; Rezaei, F. Binderless zeolite monoliths production with sacrificial biopolymers. *Chem. Eng. J.* **2021**, *407*, 128011.

(23) Yu, L.; Gong, J.; Zeng, C. F.; Zhang, L. X. Synthesis of Binderless Zeolite X Microspheres and Their CO2 Adsorption Properties. *Sep. Purif. Technol.* **2013**, *118*, 188−195.

(24) Yan, B.; Yu, S.; Zeng, C. Binderless zeolite NaX microspheres with enhanced CO2 adsorption selectivity. *Microporous Mesoporous Mater.* **2019**, *278*, 267−274.

(25) Yu, L.; Gong, J.; Zeng, C.; Zhang, L. Synthesis of Monodisperse Zeolite A/Chitosan Hybrid Microspheres and Binderless Zeolite A Microspheres. *Ind. Eng. Chem. Res.* **2012**, *51*, 2299−2308.

(26) Sun, H.; Sun, Z.; Shen, B.; Liu, J.; Li, G.; Wu, D.; Zhang, Y. One-pot synthesis of binderless zeolite A spheres via in situ hydrothermal conversion of silica gel precursors. *AIChE J.* **2018**, *64*, 4027−4038.

(27) Sun, M. H.; Chen, L. H.; Yu, S.; Li, Y.; Zhou, X. G.; Hu, Z. Y.; Sun, Y. H.; Xu, Y.; Su, B. L. Micron-Sized Zeolite Beta Single Crystals

Featuring Intracrystal Interconnected Ordered Macro-Meso-Microporosity Displaying Superior Catalytic Performance. *Angew. Chem., Int. Ed.* **2020**, *59*, 19582.

(28) Rasmussen, K. H.; Goodarzi, F.; Christensen, D. B.; Mielby, J.; Kegnæs, S. Stabilization of Metal Nanoparticle Catalysts via Encapsulation in Mesoporous Zeolites by Steam-Assisted Recrystallization. *ACS Appl. Nano Mater.* **2019**, *2*, 8083−8091.

(29) Meloni, M.; Runnebaum, R. C. Tuning Supported Ni Catalysts By Varying Zeolite Beta Heteroatom Composition: Effects On Ethylene Adsorption And Dimerization Catalysis. *Catal. Sci. Technol.* **2021**, *11*, 3393−3401.

(30) van der Graaff, W. N. P.; Li, G.; Mezari, B.; Pidko, E. A.; Hensen, E. J. M. Synthesis of Sn-Beta with Exclusive and High Framework Sn Content. *ChemCatChem* **2015**, *7*, 1152.

(31) Manookian, B.; Hernandez, E. D.; Baer, M. D.; Mundy, C. J.; Jentoft, F. C.; Auerbach, S. M. Experimental and DFT Calculated IR Spectra of Guests in Zeolites: Acyclic Olefins and Host-Guest Interactions. *J. Phys. Chem. C* **2020**, *124*, 10561.

(32) Liu, J. X.; He, N.; Liu, C. Y.; Wang, G. R.; Xin, Q.; Guo, H. C. Engineering the porosity and acidity of H-Beta zeolite by dealumination for the production of 2-ethylanthraquinone via 2-(4′-ethylbenzoyl)benzoic acid dehydration. *RSC Adv.* **2018**, *8*, 9731.

(33) Li, Z.; Jiang, X.; Xiong, G.; Nie, B.; Liu, C.; He, N.; Liu, J. Towards The Preparation Of Binderless ZSM-5 Zeolite Catalysts: The Crucial Role Of Silanol Nests. *Catal. Sci. Technol.* **2020**, *10*, 7829.

(34) Zhao, R.; Zhao, Z.; Li, S.; Zhang, W. Insights into the Correlation of Aluminum Distribution and Brönsted Acidity in H-Beta Zeolites from Solid-State NMR Spectroscopy and DFT Calculations. *J. Phys. Chem. Lett.* **2017**, *8*, 2323−2327.

(35) Zhang, Y.; Li, M.; Xing, E.; Luo, Y.; Shu, X. Protective desilication of highly siliceous H-ZSM-5 by sole tetraethylammonium hydroxide for the methanol to propylene (MTP) reaction. *RSC Adv.* **2018**, *8*, 37842.

(36) Liu, J.; Wang, J.; Zhou, W.; Miao, C.; Xiong, G.; Xin, Q.; Guo, H. Construction of an operando dual-beam fourier transform infrared spectrometer and its application in the observation of isobutene reactions over nano-sized HZSM-5 zeolite. *Chin. J. Catal.* **2017**, *38*, 13−19.